J. Fluid Mech. (2009), *vol.* 633, *pp.* 271–283.
doi:10.1017/S0022112009007642 Printed in the United Kingdom

An experimental investigation of incipient spilling breakers

J. D. DIORIO, X. LIU AND J. H. DUNCAN†

Department of Mechanical Engineering, University of Maryland, College Park, MD 20742, USA

(Received 18 August 2008 and in revised form 10 April 2009)

In the present paper, the profiles of incipient spilling breaking waves with wavelengths ranging from 10 to 120 cm were studied experimentally in clean water. Short-wavelength breakers were generated by wind, while longer-wavelength breakers were generated by a mechanical wavemaker, using either a dispersive focusing or a sideband instability mechanism. The crest profiles of these waves were measured with a high-speed cinematic laser-induced fluorescence technique. For all the wave conditions reported herein, wave breaking was initiated with a capillary-ripple pattern as described in Duncan *et al.* (*J. Fluid Mech.*, vol. 379, 1999, pp. 191–222). In the present paper, it is shown that at incipient breaking the crest shape is self-similar with two geometrical parameters that depend only on the slope of a particular point on the front face of the gravity wave. The scaling relationships appear to be universal for the range of wavelengths studied herein and hold for waves generated by mechanical wavemakers and by wind. The slope measure is found to be dependent on the wave phase speed and the rate of growth of the crest height prior to incipient breaking.

1. Introduction

It is well known that breaking waves enhance the rates of transfer of mass, momentum and energy across the air–sea interface by creating turbulence, water droplets and air bubbles. The wave shape and flow field at the point at which breaking begins, defined here as the transition from laminar flow to turbulent flow, are critical aspects of the dynamics of breaking waves. Though there has been considerable research on breaking waves (see the reviews by Banner & Peregrine 1993; Thorpe 1995; Melville 1996; Duncan 2001), a general incipient breaking condition has been elusive. The most successful work has been with steady waves. This work began with Stokes (1847) who showed that the limiting form of the crests of a steady periodic gravity wavetrain is a corner flow with an included angle of 120° and a stagnation point at the crest. Duncan (1983) found that steady waves produced by towing a two-dimensional hydrofoil at constant depth, angle of attack and speed would continue to break once disturbed if the slope of the wave's forward face was greater than 17°. The stagnation point idea was also used by Banner & Phillips (1974) in considering the effect of a surface wind drift layer on the breaking criterion for a steady wave. In experiments with hydrofoil-produced waves and a turbulent surface wake, Miller *et al.* (1999) found that the breaking criterion had the same functional form as in the theory of Banner & Phillips (1974) but was reached when the flow speed at the crest was 50 % of the wave phase speed.

† Email address for correspondence: duncan@umd.edu

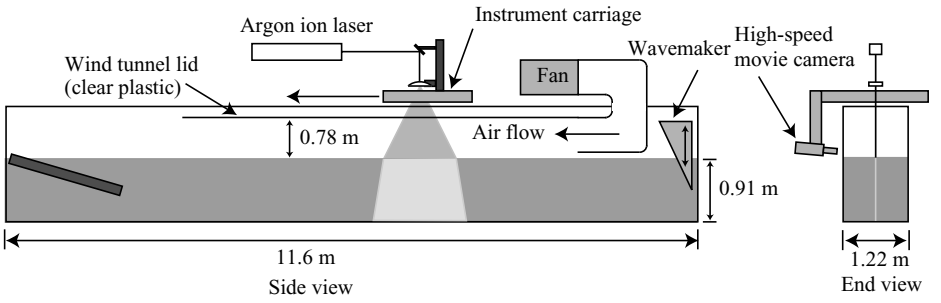

FIGURE 1. Schematic of wave tank with wavemaker, wind tunnel and instrument carriage.

Work to determine a breaking criterion for unsteady waves has been less successful. This is partly because the wave goes through a range of shapes as it breaks, and both the theory and the experiments are more difficult than in steady waves. Recent work in this area includes the studies of Banner & Peirson (2007), Banner & Song (2002) and Song & Banner (2002), which focus on waves breaking within modulating wave packets. These studies emphasize the role of the rate of increase of energy at the maximum height of the wave packet envelope on incipient conditions and the breaker type (spilling to plunging). Also, Tulin & Landrini (2001) have found through numerical calculations that in deep-water modulating gravity wavetrains, a wave crest will evolve quickly to breaking whenever the local maximum particle speed exceeds one-half of the phase velocity of the dominant wavetrain. The relationship between this latter breaking criterion for unsteady waves and that of Miller *et al.* (1999) for steady waves is not known, even though both occur when the particle speed reaches one-half of the wave phase speed.

In the present work, the results of experiments focused on the crest shapes of unsteady spilling breaking waves at the point of incipient breaking are reported. Both mechanically generated and wind-generated waves are studied, and the total range of wavelengths is from 10 to 120 cm. This work is reported in the following three sections: § 2 'Experimental details', § 3 'Results and discussion' and § 4 'Conclusions'.

2. Experimental details

2.1. *Wave tank*

The experiments were carried out in a wind-wave tank that is 11.6 m long, 1.22 m wide and 2.1 m deep with a water depth of 0.91 m (see figure 1). The tank includes a programmable wavemaker consisting of a vertically oscillating wedge located at one end of the tank and a programmable instrument carriage that rides above the tank. Both the wavemaker and the carriage are controlled by the same computer so that coordinated motions can be obtained. Further details about the wavemaker and carriage can be found in Duncan *et al.* (1999).

The tank also includes a wind tunnel. The tunnel is powered by two 5.6 kW fans that are mounted to the ceiling of the laboratory and drive air towards the wavemaker. An entrance section consisting of ducting, two sets of turning vanes, three screens and a honeycomb is used to condition and redirect the air flow so that it moves parallel to the water surface in the direction away from the wavemaker. The sidewalls of the test section of the wind tunnel are part of the water tank, and the lid is made of clear acrylic. The lid is positioned 0.78 m above the mean water level and ends about 1 m before the end of the tank to allow the air to exit. The bottom of the entrance section

Case number	Number of runs	f_0 (Hz)	λ_0 (cm)	A/λ_0
1	3	1.15	118.06	0.0505
2	1	1.26	98.34	0.0505
3	1	1.42	77.43	0.0505
4	1	1.42	77.43	0.0496
5	1	1.42	77.43	0.0487

TABLE 1. The parameters of the five wavemaker motions used with the dispersive-focusing technique. In this table, f_0 is the average frequency of the wave packet; $\lambda_0 = g/(2\pi f_0{}^2)$ is the wavelength of the average frequency according to linear theory; and A/λ_0 is the non-dimensional amplitude of the wavemaker motion. Note that the first case was done three times, yielding seven experiments in total.

of the wind tunnel is 10.2 cm above the mean water level. This gap allows waves generated by the wavemaker to enter the tank. The area between the wavemaker and the back of the wind tunnel is sealed with flexible material in order to minimize reverse air flow under the entrance section. A beach comprised of a horsehair mat on a tilted acrylic plate was located at the far end of the tank below the wind tunnel exit to damp wave reflections. A skimmer/filtration system was turned on between experimental runs to minimize surfactant levels in the tank (see Duncan *et al.* 1999).

2.2. *Wave generation*

Waves were generated using three different methods. The first method was a dispersive focusing technique (Longuet-Higgins 1974; Rapp & Melville 1990), and the wavemaker motion parameters were nearly the same as those described in Duncan *et al.* (1999). Five wavemaker motions were used with this method, and the average wave packet frequency f_0 and the non-dimensional amplitude of the wavemaker motions A/λ_0 (where A is the overall amplitude and $\lambda_0 = g/(2\pi f_0{}^2)$ is the wavelength of the average frequency according to linear wave theory) can be found in table 1. In the second method, the wavemaker was used to generate a sinusoidal wavetrain of initial frequency f_0 and initial slope a_0k, where a_0 is the wave amplitude and k the wavenumber. Superimposed on this sinusoidal motion were unstable sideband wave components at frequencies slightly above and below the frequency of the main wavetrain. The most unstable sideband frequencies are located at $f_\pm = f_0(1 \pm \beta a_0 k)$, where the dependence of the constant β on a_0k has been determined theoretically (Benjamin & Feir 1967; Longuet-Higgins 1978) and verified by experiments (Lake *et al.* 1977; Melville 1982). In the present case, β was taken as 0.75 based on measurements of the sideband frequencies that appeared for wavetrains generated with only the primary wave component in our facility. The sideband frequencies are superimposed on the main wavetrain at an amplitude of αa_0, where $\alpha \ll 1$. The values of the parameters used in this method are summarized in table 2. In the third method, the wind was used to generate waves. The wind speed at the centre of the wind tunnel cross-section ranged from 6.0 to 7.2 m s^{-1}, and the fetches at the location of incipient breaking ranged from 3 to 5.5 m from the wind tunnel entrance in the present study. Capacitance-type wave-height gauges were used to measure the dominant wave frequencies. The peak frequencies ranged from roughly 2.5 to 3.5 Hz, which, via linear theory, yield wavelengths in the range of 10–25 cm. In all, measurements from 18 different breakers are reported herein (7 generated by dispersive focusing, 3 generated by sideband instabilities and 8 generated by wind).

Number of runs	f_0 (Hz)	a_0k	f_+ (Hz)	f_- (Hz)	α
3	2.3	0.30	2.81	1.79	0.015

TABLE 2. The parameters used for the three waves generated using the sideband instability mechanism. In this table, f_0 is the frequency of the main wavetrain; a_0k is the measured wave slope, where a_0 is the amplitude of the initially unmodulated sinusoidal wavetrain measured at a distance of 5 m from the wavemaker using a capacitance probe and k is determined from f_0 via linear theory; f_+ is the frequency of the upper sideband; f_- is the frequency of the lower sideband; α is the ratio of the sideband input amplitudes to the input amplitude of the main wavetrain.

2.3. *Wave measurement*

The profiles of the breaking waves were measured photographically with a laser-induced fluorescence (LIF) method that employs a high-speed digital movie camera. The wave crests were illuminated with a light sheet from an argon-ion laser operating at 7 W (see figure 1). The light sheet was oriented vertically along the centre plane of the tank and was 25 cm wide and 1 mm thick at the mean water level. Fluorescein dye was mixed into the tank water. The camera (Phantom v9, Vision Research) was set to record 1632×1200 pixel images with 8 bit grey levels at 250 images per second. The camera and light-sheet optics were mounted on the instrument carriage. The intersection of the light sheet and the water surface was viewed by the camera from the side and slightly above and in front of the wave crest. Wave crest profiles were extracted from each image using gradient-based edge-detection methods. A detailed description of this measurement system and the data-processing methods can be found in Duncan *et al.* (1999) and Liu & Duncan (2006).

Crest-profile measurements were taken from the instrument carriage as it moved along the tank with the crests of the breaking waves. For the cases with mechanically generated waves, the carriage motion was synchronized with the wave motion by trial and error by varying the carriage starting position, the starting time relative to the wavemaker motion, the acceleration and the final speed from run to run. For cases in which the wind was used to generate waves, the approximate phase speed of the waves was determined at the fetch of interest, and the carriage was run repeatedly at this speed. A run was considered successful when a wave was seen to break in the camera's field of view. It is emphasized that the geometrical and propagation characteristics of breaking wind waves measured at the same wind speed and fetch vary from one event to another.

3. Results and discussion

Figure 2 contains LIF images of the crest region of three waves at the point of incipient breaking (defined as the time $t = 0$ herein) during three different experiments. The images have been cropped to show a 5×2 cm region near the wave crest, and all the waves are moving from right to left. The wave in figure 2(a) was generated using the dispersive-focusing technique and has a wavelength of roughly 120 cm ($=g/(2\pi f_0^2)$, where g is the acceleration of gravity) and an amplitude of 8 cm as measured from the undisturbed water level to the crest. The wave in figure 2(b) was generated by the sideband instability method and has a wavelength of roughly 30 cm and an amplitude of 1.8 cm. The wave in figure 2(c) was generated directly by the wind and has a wavelength of approximately 13 cm and a crest height of 0.7 cm above

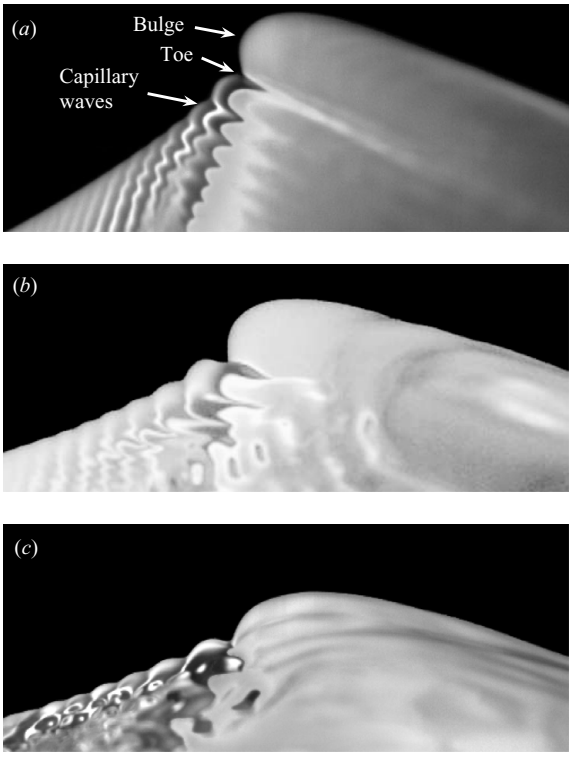

FIGURE 2. Images of wave crests at incipient breaking from high-speed movies in three separate experiments. Each image shows a 5×2 cm section near the wave crest, and the waves are moving from right to left. Each wave was generated using a different method and has a different wavelength (λ) and amplitude (a). (a) Dispersive focusing, $\lambda = 120$ cm, $a = 8$ cm. (b) Sideband instability, $\lambda = 30$ cm, $a = 1.8$ cm. (c) Wind driven, $\lambda = 13$ cm, $a = 0.7$ cm. The wavy boundary between the black region at the top of each image and the non-uniform grey region below is the wave crest profile at the intersection of the light sheet and the water surface. The pattern seen below this boundary is the result of two refraction processes: the first as the light sheet enters the water creating a non-uniform pattern in the fluorescein dye and the second as the non-uniform light intensity in the glowing dye within the light sheet is viewed through the water surface between the camera and the light sheet. More details can be found in Duncan *et al.* (1999).

the mean water level in the tank before the wind is turned on. As can be seen from the figure, a capillary-bulge pattern appears in all the images (see figure 2*a* for the nomenclature). This pattern includes a round bulge formed on the forward (left) face of the wave crest and a train of capillary waves upstream (to the left) of the leading edge (toe) of the bulge. At the instant in time after the images shown, the toe, which was stationary relative to the wave crest prior to these images, begins to move down the wave face, and a turbulent flow ensues (see Duncan *et al.* 1999; Qiao & Duncan 2001).

Figure 3(a) shows the wave crest profiles taken from the images in figure 2. In this plot, the profiles are aligned at the toe point to remove the large differences in wave crest height and thereby allow better comparison of the crest profiles. As can be seen from the figure, though the profiles are qualitatively similar, the variations in the slopes of the free surface upstream of the toe and the curvature of the bulge are quite pronounced. Generally speaking, both of these quantities increase with the

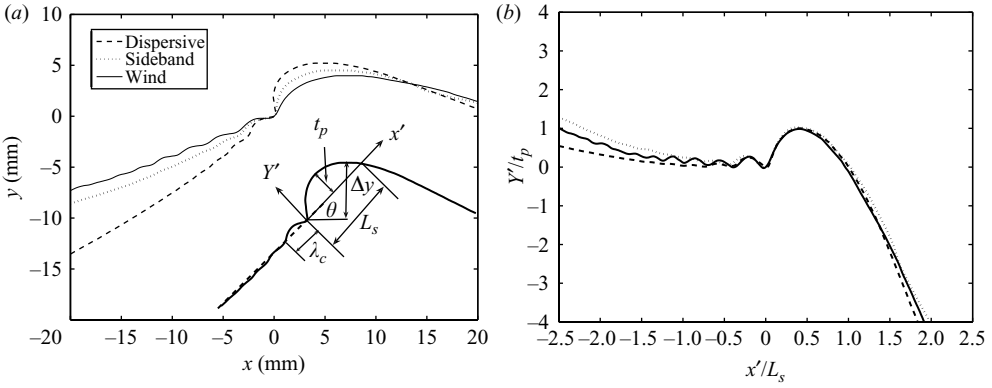

FIGURE 3. Crest profiles of the three waves shown in figure 2. (*a*) After aligning the profiles at the toe point. (*b*) After rotating each profile so that the slope of the front face at the toe is horizontal and after scaling the horizontal and vertical axes by L_s and t_p, respectively (see the caption in *a*).

wavelength of the breaking wave. This trend in local surface slope is qualitatively similar to the theory of Longuet-Higgins (1996). In the theory, a capillary jump, which forms the capillary-bulge system, occurs at the point on the wave profile at which the flow speed in the reference frame of the crest equals the minimum phase speed of capillary–gravity waves and the gradient of the flow speed at the surface is high. Longuet-Higgins (1996) has shown that the surface slope at the location of this point decreases with decreasing gravity wavelength. The profile shapes shown in figure 3(*a*) are qualitatively similar to those found in numerical calculations of short-wavelength steep waves as reported by Mui & Dommermuth (1995), Fedorov & Melville (1998), Fedorov, Melville & Rozenberg (1998), Tulin (1996) and Longuet-Higgins & Dommermuth (1997).

In order to compare the profile shapes quantitatively, a few geometric parameters are defined. These parameters include the vertical distance Δy from the maximum height of the profile to the toe point, the length of the first capillary wave (λ_c) upstream of the toe, a mean surface slope at the toe (m), a bulge length (L_s) and a bulge thickness (t_p) (see the insert in figure 3*a*) . In order to obtain values for m, a polynomial (anywhere from the second to the fourth order) was fitted to the front wave face from the toe to a point 3 cm upstream of the toe. This polynomial was forced to pass through the toe point which is defined numerically as the point in the profile with maximum upward curvature. The purpose of this polynomial is to follow the overall shape of the front face of the gravity wave near the crest while ignoring the undulations due to the capillary waves. A typical fit is shown in the inset of figure 3(*a*). The slope of this polynomial at the toe point is then chosen as $m = \tan\theta$ (see the insert in figure 3*a* for the definition of θ). The values of m measured in this study were found to be between 0.3 and 1.5, which correspond to $\theta = 17°$–$56°$. (Note that θ at the crest of a limiting form Stokes wave is 30°.) The length of the bulge L_s is defined as the distance from the toe to the crest profile following a straight line with slope m. The bulge thickness t_p is defined as the maximum perpendicular distance from the line forming L_s to the surface of the bulge.

Using the parameters m, L_s and t_p measured for each wave at incipient breaking, the crest profiles are plotted in figure 3(*b*) in the local scaled coordinate system X'/L_s–Y'/t_p, where X' is directed from the toe along the line L_s and Y' is perpendicular

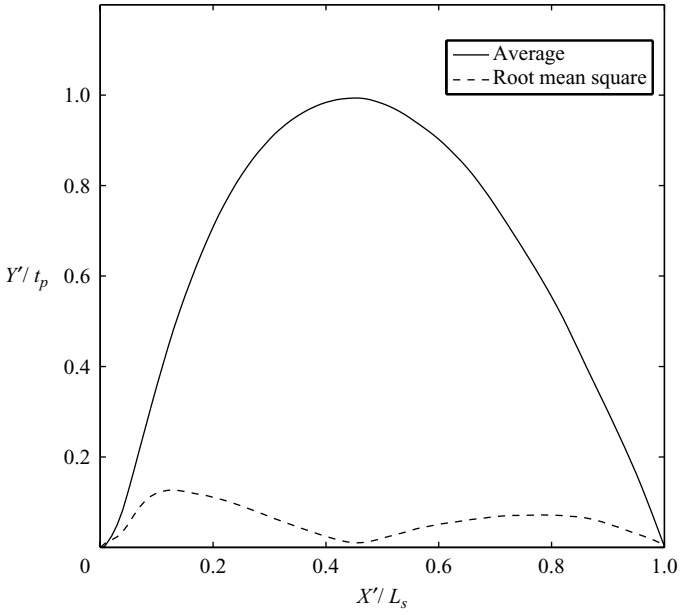

FIGURE 4. Average and standard deviation of the scaled and rotated bulge profiles for all 18 waves studied herein.

to X'. When viewed in this non-dimensional way, the similarity of the profiles in the crest region is quite interesting, considering the large differences in gravity wave amplitude, wavelength and generation method. The scaled crest profiles for all the other incipient breaking waves studied herein are similar to these but are not shown here in order to make the plot clearer. Instead, a plot of the average scaled profile and the standard deviation distribution computed from all 18 waves is shown in figure 4. The mean profile has a single maximum at $X' \approx 0.42 L_s$ and goes to zero at $X' = 0$ and L_s. The standard deviation reaches a peak of 12 % on the front face of the wave; however, careful analysis of the processing techniques indicates that much of this variation can be attributed to the selection of the incipient breaking frame and the toe position. The incipient breaking frame is difficult to define because it is the frame before the toe starts moving from rest. Thus, its initial motion between frames is quite small. The toe position is taken as the point of maximum upward curvature of the profile. While its determination is done with a consistent numerical procedure, the result is sometimes a little off the position one might choose by eye. The primary effect of changing both the incipient breaking image frame and the toe position is a slight horizontal shift of the peak in the profile. This results in a right–left shift of the nearly vertical parts of the profile near $X'/L_s = 0$ and 1, thus creating the large standard deviations there.

The parameters L_s and t_p are plotted versus m in figures 5(a) and 5(b), respectively. As can be seen in figures 5(a), the data appears to follow a single curve, independent of the method used to generate the wave. The curve has a negative slope that decreases with increasing m. The values of t_p (figure 5b) show a fair amount of scatter, but generally t_p decreases with increasing m. This scatter is created primarily because t_p is a very small quantity that changes rapidly as the waves approach breaking and because errors in the slope m cause changes in t_p.

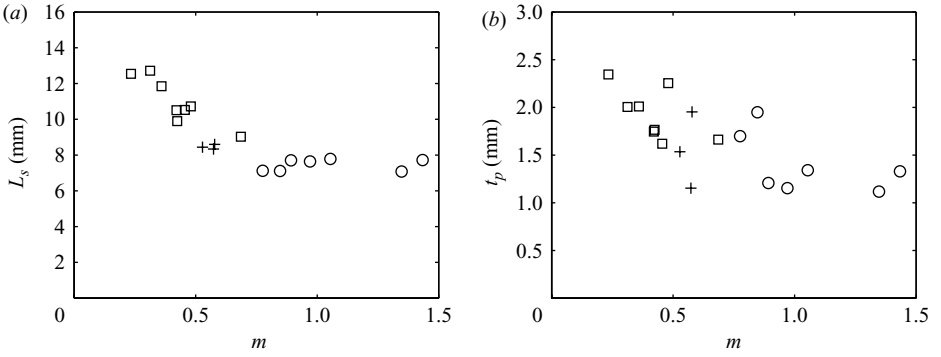

FIGURE 5. Plots showing the variation of L_s (a) and t_p (b) with the local slope parameter, m: □, wind waves; +, sideband waves; and ○, focused waves.

In the numerical calculations for steady waves ($\lambda \approx 0.5$ m) in a liquid with a very high surface tension (9 and 16 times the surface tension of water) presented in Longuet-Higgins (1996), the shape of the bulge and, of course, lengths describing the capillary-ripple system scale only with the gravity–capillary wavelength $2\pi(\gamma/g)^{0.5}$, where γ is the surface tension coefficient (σ/ρ) (see figure 18 in Longuet-Higgins 1996). A similar result was found in the experiments of Duncan *et al.* (1999) for unsteady mechanically generated breakers with wavelengths ranging from 70 to 118 cm (see their figure 23). In contrast, the present results, which cover a wide range of wavelengths and a single value of $2\pi(\gamma/g)^{0.5}$, indicate that L_s and t_p increase substantially as m decreases. However, it should be noted that at the higher values of m, where the wavelengths are the same as those studied in Duncan *et al.* (1999), L_s and t_p are relatively constant.

Using the measured Δy data, estimates of the underlying flow speed (q_t) at the toe point were obtained by using the steady Bernoulli equation and by assuming that there is a stagnation point at the crest of the wave. (While the flow is clearly unsteady and there is no experimental verification of the stagnation point at the crest, the above assumptions are used here in an attempt to gain some understanding of the flow and capillary waves; see below.) The result is $q_t = \sqrt{2g\Delta y}$, where g is the acceleration due to gravity. A plot of the estimated values of q_t versus wave slope m is shown in figure 6(a). A linear fit to the data yields a y-intercept of roughly 25 cm s^{-1}. This value is close to the minimum phase speed of gravity–capillary waves, i.e. 23 cm s^{-1}.

When possible, measurements were also made of the wavelength of the primary capillary wave upstream of the toe, λ_c. A plot of λ_c versus m is shown in figure 6(b). (Due to a lack of spatial resolution and camera angle in some movies, measurements of λ_c are not available for several of the dispersively focused wave cases.) The measured values of λ_c range from about 5 to 4 mm, decreasing slightly with increasing m. Because these capillary waves are stationary relative to the crest, the phase speed of these waves relative to still water must equal q_t. Using the estimated values of q_t from figure 6(a), capillary wavelengths were calculated using both the linear dispersion relationship for gravity–capillary waves ($q_t^2 = c^2 = g/k + \gamma k$, where $k = 2\pi/\lambda_c$, $\gamma = \sigma/\rho$, σ is the surface tension and ρ is the density of the liquid) and the nonlinear dispersion relationship for capillary waves of maximum amplitude ($q_t^2 = c^2 = 0.657\gamma k$, from Crapper 1957). (To our knowledge there is no analytical solution for the nonlinear dispersion relationship for gravity–capillary waves of maximum amplitude.) The results from these calculations are also shown in figure 6(b). As can be seen from the figure, in spite of the approximate nature of the theory, the wavelengths calculated

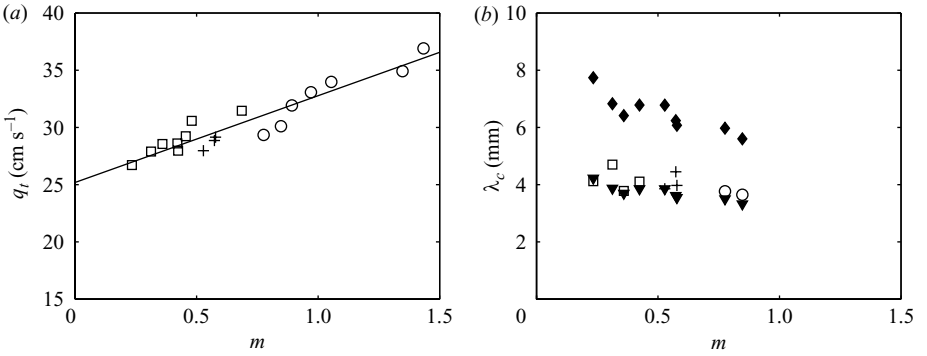

FIGURE 6. Measurements and analysis of the length of the first capillary wave upstream of the toe, λ_c. (*a*) The flow speed at the toe q_t (as calculated from the measured Δy and Bernoulli's equation) versus local slope parameter m. The straight line is a least squares fit to the data. (*b*) The wavelength (λ_c) of the first capillary wave upstream of the toe versus m; □, wind waves; +, sideband instability waves; ○, focused waves; ◆, linear gravity–capillary wave theory; and ▼, nonlinear capillary wave theory (maximum amplitude). (Due to a lack of spatial resolution in some images, measurements of λ_c were not made for several of the dispersively focused wave cases.)

using the linear and nonlinear dispersion relationships bracket the measured values of λ_c with the estimates from the nonlinear dispersion relationship providing the best match.

The above results have shown the importance of the slope parameter m in determining the wave crest shape at incipient breaking. The next question is what determines m for a given breaker? Here we explore the hypothesis that m at incipient breaking is a function of both the phase speed c and the rate of change of the crest height just prior to breaking. The phase speed is chosen because it is related to the wavelength, and as discussed above, it appears on both theoretical and experimental grounds that m decreases with decreasing wavelength. (In the present experiments, the wavelength was not measured; however, the phase speed was measured directly by determining the speed of the crest as seen in the movies and then adding the known speed of the instrument carriage.) The wave phase speeds fell in the range of 50–70 cm s^{-1} for waves generated by the wind and the sideband instability mechanism and in the range 90–120 cm s^{-1} for the waves generated using dispersive focusing.

A useful measure of the rate of change of wave height at breaking is difficult to determine. This is because the rate of change of wave height, while strongly positive in the early stages of the approach to breaking, is close to zero (in some cases even slightly negative) at incipient breaking for many of the waves. Based on data for the dispersively focused breakers as shown in the Appendix, an average wave crest growth rate $P = [y_m(0) - y_m(-0.23T)]/(0.23T)$ is used in the present work. (On intuitive grounds, a time of $0.25T$ was desired for this measurement; however, it turned out that $0.23T$ was the maximum value that could be used in the analysis of the largest number of high-speed movies.) The values of P were then divided by the corresponding values of c to give an average dimensionless growth rate, which is essentially the rate of change of wave slope with dimensionless time t/T. Also, the values of c were divided by the minimum phase speed of gravity–capillary waves, $c_{min} = \sqrt{2}(g\gamma)^{0.25} = 23.1$ cm s^{-1}, with $\sigma = 73$ mN m^{-1}. A least squares fit of a second-order polynomial ($m = f(c/c_{min}, P/c)$) to the data set was performed, and the resulting contour plot of m on the c/c_{min}–P/c plane is given in figure 7. The data points on the plot are colour coded on the same scale as the contours so that the accuracy of

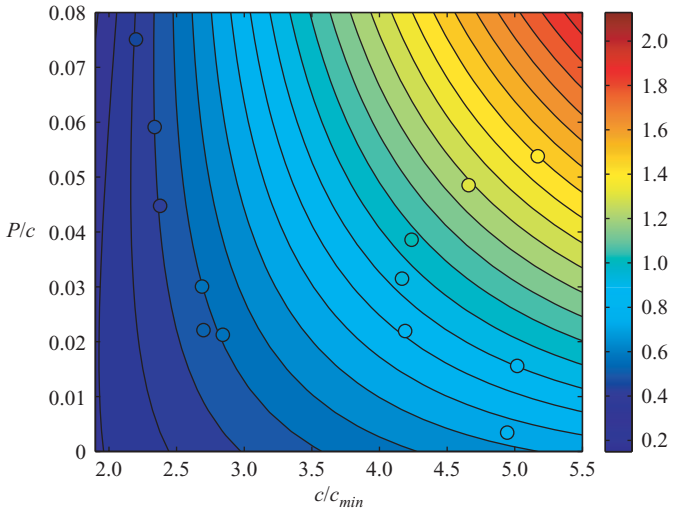

FIGURE 7. Contour plot of the slope m as a function of the dimensionless wave phase speed (c/c_{min}, where c_{min} is the minimum gravity–capillary wave phase speed $\sqrt{2}(g\gamma)^{0.25}$, where g is the acceleration of gravity and $\gamma = \sigma/\rho$ with σ the surface tension, taken as 73 dyn cm^{-1} and ρ the density, taken as 1 gm cm^{-3}) and the non-dimensional average growth rate P/c. The contours are from a least squares fit of a second-order polynomial, $m = f(c/c_{min}, P/c)$, to the data. The shape of the contours is only supported by the experiments in the vicinity of the data points. The face colour of each data point indicates its value of m according to the colour legend on the right. Five of the data points for wind waves were not included in these plots because random surface fluctuations or insufficient movie frames prior to breaking prevented obtaining P by the method used here (see the appendix).

the fit can be estimated from visual inspection. The root-mean-square error from the fit is 5.5 % of the average of the measured values of m, indicating that the concept that m is a function of c and P/c has some validity. From this plot, it can be seen that for low wave phase speeds (shorter wavelengths) the growth rate has little effect on m, while for the highest phase speeds, m increases significantly with growth rate. This result is in agreement with our intuition that long waves with rapidly increasing amplitude become strong breakers. In particular, plunging breakers were not produced in the wind-generated and sideband instability waves, which have relatively short wavelength, while with appropriate wave generation parameters, plunging breakers (where the local surface slope becomes vertical during the approach to breaking) can be generated at longer wavelengths with the dispersive-focusing technique.

The dimensionless crest height growth rate P/c used here should be distinguished from the parameter μ used by Banner & Peirson (2007), Banner & Song (2002) and Song & Banner (2002), which is the average dimensionless growth rate of the local energy density at the peak of the wave packet envelope. The parameter μ is related to the evolution of the wave packet envelope, while P/c is the rate of change of amplitude of a single wave crest as it moves through a packet.

4. Conclusions

The crest profiles of spilling breakers with wavelengths in the range of 10–120 cm were investigated experimentally. These waves were generated with a mechanical

wavemaker and with wind. It was found that the bulge-capillary wave system that appears on the forward faces of short-wavelength spilling breakers is qualitatively similar for all the waves studied herein. The bulge was found to have a self-similar shape with its length and thickness as scaling parameters, which in turn are found to be functions of the slope (m) of the mean water surface just upstream of the leading edge (toe) of the bulge. This scaling seems to be independent of wave generation method, leading one to believe that at least some features of mechanically generated and wind waves are quite similar. It was found that m is a function of the wave phase speed and the average growth rate (P) of the wave amplitude before breaking begins. The data indicates that for the low-phase-speed waves m is independent of P, while for the higher-phase-speed waves m increases with increasing growth rate. Finally, estimates of the length of the first capillary wave upstream of the toe that were made using a simple theory based on estimates of the flow speed at the toe and the capillary–gravity wave dispersion relationship compared well with the measured values. The results of this study show that breaking is a multi-scale nonlinear phenomenon in which the local gravity wave (10–120 cm wavelength) slope controls the surface-tension-dominated crest shape (≈ 1 cm wavelength). The fact that the scaling parameters are unaffected by wind supports the theory (Longuet-Higgins 1992) that the dynamics of the capillary-ripple pattern at the crest are dominated by energy transfer from the gravity wave. Also, Fedorov *et al.* (1998) found that the capillary-ripple patterns in wave profiles computed with surface pressure forcing (simulating the effect of wind) and those found in laboratory experiments with mechanically generated waves with lengths $\approx$ 5–10 cm show remarkable similarity.

The support of the Division of Ocean Sciences, National Science Foundation, under grant OCE751853 is gratefully acknowledged. JDD acknowledges the support of an ARCS Foundation fellowship. Measurements of the sideband frequencies in our wave tank were performed by Gunther Seer.

Appendix. Wave growth rate

To illustrate the choice of the average growth rate P consider the wave crest height versus time data for focused breakers plotted in figure 8. In this plot, the crest height y_m is non-dimensionalized by its maximum value for each wave, and the time t is non-dimensionalized by the average wave frequency (tf_0) with $t = 0$ the time of incipient breaking. Data is shown for the seven dispersively focused waves. As can be seen from the plot, the instantaneous rate of change of dimensionless crest height is nearly zero at incipient breaking for all the waves. However, the wide range of changes in height over the time period say from $tf_0 = -0.2$ to $tf_0 = 0$ for the various waves indicates a wide range in average rate of growth. The data in figure 8 is consistent with the wave crest travelling through a wave packet envelope and breaking when the wave reaches the position of the maximum height of the envelope. The crest height data for the sideband waves and some of the wind waves show similarly shaped curves.

Values of P could not be computed for five of the wind waves. The problem in computing P for these waves stems from the fact that wind waves break at random times and locations and that they interact with other wave components during breaking. Because they occur randomly, it is difficult to get a full movie of the breaking event (see the description of the procedure for obtaining movies of these waves at the end of § 2). Thus, in some of the waves there was no photographic record of the breaking event for the required 0.23 wave periods prior to incipient breaking.

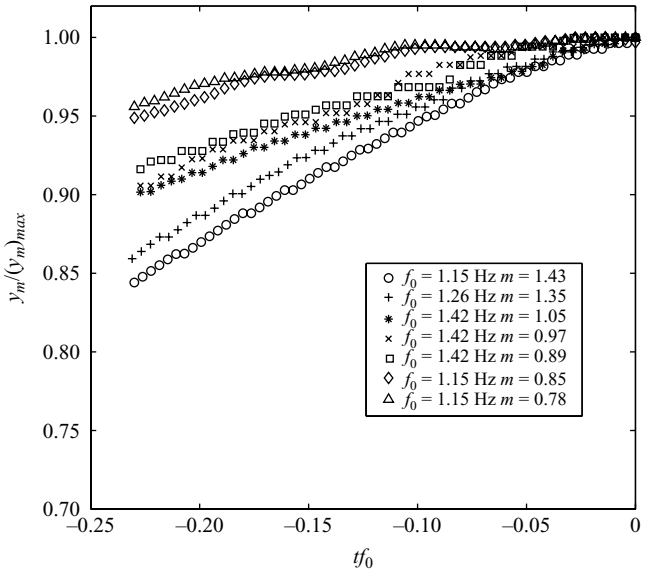

FIGURE 8. Non-dimensional height $(y_m(t)/(y_m)_{max})$ versus non-dimensional time (tf_0) for the dispersively focused breakers, where $y_m(t)$ is the wave height at any time t with $t = 0$ the time of incipient breaking; $(y_m)_{max}$ is the wave height at incipient breaking; and f_0 is the average frequency of the wave packet.

The interaction of the breaker with other wave components is seen in the movies as the pre-breaking crest moves over small slow-moving wave components. Sometimes the breaking event is triggered by this interaction. While the crest shape data at the incipient condition was included in the geometry parameter plots for these breaking events, a growth rate could not be obtained, since these waves can break even when the crest height has been constant or decreasing up to the point at which the long wave interacts with the short wave. Our relationship between c/c_{min}, P/c and m is not valid for these waves, since the breaking mechanism does not involve a continuous increase in amplitude leading up to incipient breaking. It is interesting that even for these breaking events, the geometrical parameters describing their crest shape fall on the same curve when plotted versus m as the data from the other waves.

REFERENCES

BANNER, M. L. & PEIRSON, W. L. 2007 Wave breaking onset and strength for two-dimensional deep-water wave groups. *J. Fluid Mech.* **585**, 93–115.

BANNER, M. L. & PEREGRINE, D. H. 1993 Wave breaking in deep-water. *Annu. Rev. Fluid Mech.* **25**, 373–397.

BANNER, M. L. & PHILLIPS, O. M. 1974 Incipient breaking of small-scale waves. *J. Fluid Mech.* **65**, 647.

BANNER, M. L. & SONG, J. B. 2002 On determining the onset and strength of breaking for deep water waves. Part 2. Influence of wind forcing and surface shear. *J. Phys. Oceanogr.* **32** (9), 2559–2570.

BENJAMIN, T. B. & FEIR, J. E. 1967 The disintegration of wave trains on deep water. Part 1. Theory *J. Fluid Mech.* **27**, 417–430.

CRAPPER, G. D. 1957 An exact solution for progressive capillary waves of arbitrary amplitude. *J. Fluid Mech.* **6**, 532–540.

Duncan, J. H. 1983 The breaking and nonbreaking wave resistance of a two-dimensional hydrofoil. *J. Fluid Mech.* **126**, 507–520.

Duncan, J. H. 2001 Spilling breakers. *Annu. Rev. Fluid Mech.* **33**, 519–547.

Duncan, J. H., Qiao, H., Philomin, V. & Wenz, A. 1999 Gentle spilling breakers: crest profile evolution. *J. Fluid Mech.* **379**, 191–222.

Fedorov, A. V. & Melville, W. K. 1998 Nonlinear gravity–capillary waves with forcing and dissipation. *J. Fluid Mech.* **354**, 1–42.

Fedorov, A. V., Melville, W. K. & Rozenberg, A. 1998 An experimental and numerical study of parasitic capillary waves. *Phys. Fluids* **10** (6), 1315–1323.

Lake, B. M., Yuen, H. C., Rungaldier, H. & Ferguson, W. E. 1977 Nonlinear deep-water waves: theory and experiment. Part 2. Evolution of a continuous wavetrain. *J. Fluid Mech.* **83**, 49–74.

Liu, X. & Duncan, J. H. 2006 An experimental study of surfactant effects on spilling breakers. *J. Fluid Mech.* **567**, 433–455.

Longuet-Higgins, M. S. 1974 Breaking waves in deep or shallow water. In *Tenth Symposium on Naval Hydrodynamics*, Cambridge, MA.

Longuet-Higgins, M. S. 1978 Instabilities of gravity-waves of finite-amplitude in deep-water. Part 2. Subharmonics. *Proc. R. Soc. Lond.* A **360**, 489–505.

Longuet-Higgins, M. S. 1992 Capillary rollers and bores. *J. Fluid Mech.* **240**, 659–679.

Longuet-Higgins, M. S. 1996 Capillary jumps on deep water. *J. Phys. Oceanogr.* **96**, 1957–1965.

Longuet-Higgins, M. S. & Dommermuth, D. G. 1997 Crest instabilities of gravity waves. Part 3. Nonlinear development and breaking. *J. Fluid Mech.* **336**, 33–50.

Melville, W. K. 1982 The instability and breaking of deep-water waves. *J. Fluid Mech.* **115**, 165–185.

Melville, W. K. 1996 The role of surface-wave breaking in air-sea interaction. *Annu. Rev. Fluid Mech.* **28**, 279–321.

Miller, M., Nennstiel, T., Duncan, J. H., Dimas, A. & Prostler, S. 1999 Incipient breaking of steady waves in the presence of surface wakes *J. Fluid Mech.* **383**, 285–305.

Mui, R. C. Y. & Dommermuth, D. G. 1995 The vortical structure of parasitic capillary waves. *J. Fluids Engng* **117**, 355–361.

Qiao, H. & Duncan, J. H. 2001 Gentle spiling breakers: crest flow-field evolution. *J. Fluid Mech.* **439**, 57–85.

Rapp, R. & Melville, W. K. 1990 Laboratory measurements of deep water breaking waves. *Phil. Trans. R. Soc. Lond.* A **331**, 735.

Song, J. B. & Banner, M. L. 2002 On determining the onset and strength of breaking for deep water waves. Part 1. Unforced irrotational wave groups. *J. Phys. Oceanogr.* **32** (9), 2541–2558.

Stokes, G. G. 1847 On the theory of oscillatory waves. *Trans. Camb. Phil. Soc.* **8**, 441–455. Reprinted in . **1**, 314–326.

Thorpe, S. A. 1995 Dynamical processes of transfer at the sea surface. *Prog. Oceanogr.* **35**, 315–352.

Tulin, M. P. 1996 Breaking of ocean waves and downshifting. In *Waves and Nonlinear Processes in Hydrodynamics* (ed. J. Grue, B. Gjevik & J. E. Weber), pp. 177–190. Kluwer Academic.

Tulin, M. P. & Landrini, M. 2001 Wave breaking in the ocean and around ships. In *23rd Symposium on Naval Hydrodyanamics*, Val de Reuil, France.